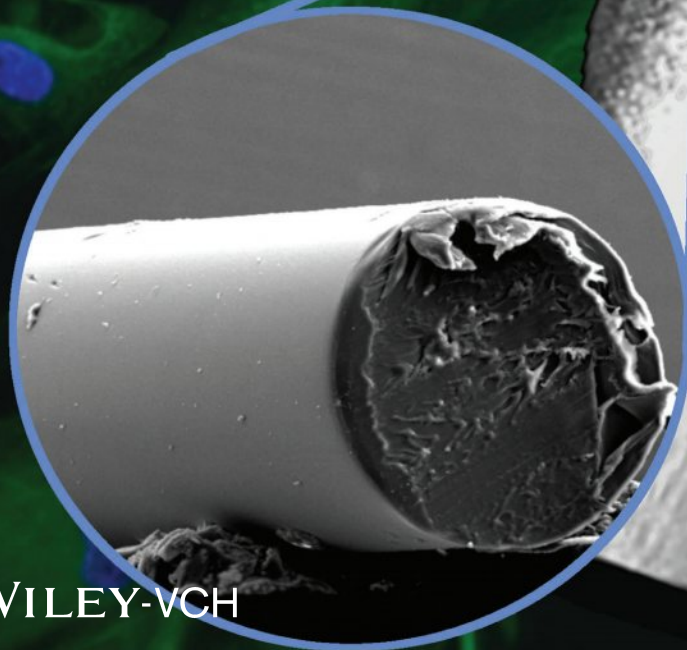


small methods



Green Light-Based Photobiomodulation with an Implantable and Biodegradable Fiber for Bone Regeneration

Yuxi Jiang, Wei Qi, Qianyi Zhang, Hao Liu, Jianyun Zhang, Ning Du, Roya Nazempour, Yuanzhe Su, Ruxing Fu, Kaiyuan Zhang, Peijun Lyu, Fan Dong, Lan Yin, Xing Sheng,* and Yuguang Wang*

Photobiomodulation (PBM) has recently started to gain popularity in clinical therapeutics. Visible light, in particular, plays a critical role in osteogenesis modulation. However, the limited penetration depth of visible light in biological tissues has constrained the application of this technology *in vivo*. Herein a green light-based PBM technique with implantable and biodegradable poly(L-lactic acid) & poly(L-lactic-co-glycolic acid) optical fibers to achieve accelerated bone regeneration is explored. Facilitated with experimental characterizations as well as numerical simulations, optical and thermal behaviors of fibers operated in the biological environment are understood. The optical regulation of bone regeneration is systematically studied both *in vitro* and *in vivo*. Under green light irradiation, biochemical activities of bone marrow-derived mesenchymal stem cells and their expression of osteogenic-related factors are significantly elevated. By introducing green light into defective bone structures via fibers in a rodent model, the process of bone regeneration and repair is accelerated. Furthermore, fibers exhibit ideal biocompatibility with both cultured cells and living tissues and undergo complete degradation *in vivo* after ≈ 1 month. Assisted with degradable optical materials and devices, such as photobiomodulation technique provides a promising solution to tissue regeneration in various biomedical applications.

1. Introduction

Bone defects are one of the most important and frequent problems in human health care, with an annual occurrence of more than 2 million worldwide.^[1] Bone defects are severe sequelae of trauma, infection, tumor resection, ageing, or congenital malformation.^[2,3] Technological developments in bone regeneration and repair can make a significant contribution to the quality of lives of patients. Methods to accelerate bone remodeling mainly include biological, chemical, and physical therapies.^[4,5] Chemical and biological methods utilize calcium ions and bone morphogenetic proteins, which have been proven to be effective for certain conditions.^[6,7] However, the concentration of chemicals is difficult to maintain; moreover, inappropriate use of medication dosage may cause cytotoxicity or internal environment disorders.^[8] In contrast to biochemical treatments that lack temporal and spatial accuracy,


Y. Jiang, W. Qi, P. Lyu, F. Dong, Y. Wang
National Engineering Laboratory for Digital
and Material Technology of Stomatology
Beijing 100081, China
E-mail: wangyuguang@bjmu.edu.cn

Y. Jiang, P. Lyu, F. Dong, Y. Wang
Center of Digital Dentistry
Peking University School and Hospital of Stomatology
Beijing 100081, China

Y. Jiang, W. Qi, P. Lyu, F. Dong, Y. Wang
National Clinical Research Center for Oral Diseases
Beijing 100081, China

Y. Jiang, W. Qi, P. Lyu, F. Dong, Y. Wang
Beijing Key Laboratory of Digital Stomatology
Beijing 100081, China

W. Qi
Department of General Dentistry
Peking University School and Hospital of Stomatology
Beijing 100081, China

 The ORCID identification number(s) for the author(s) of this article can be found under <https://doi.org/10.1002/smt.201900879>.

DOI: 10.1002/smt.201900879

Q. Zhang, R. Fu, Prof. L. Yin
School of Materials Science and Engineering
Tsinghua University
Beijing 100084, China

H. Liu, N. Du
Central Laboratory
Peking University School and Hospital of Stomatology
Beijing 100081, China

J. Zhang
Department of Oral Pathology
Peking University School and Hospital of Stomatology
Beijing 100081, China

R. Nazempour, Y. Su, K. Zhang, Prof. X. Sheng
Department of Electronic Engineering
Beijing National Research Center for Information Science
and Technology
Tsinghua University
Beijing 100084, China
E-mail: xingsheng@tsinghua.edu.cn

Prof. X. Sheng
IDG/McGovern Institute for Brain Research
Tsinghua University
Beijing 100084, China

physical methods exclusively stimulate target areas, potentially providing more precise therapies for tissue regeneration and rehabilitation.^[9] For example, heat, ultrasound, magnetic fields, and optical stimulations have been demonstrated to successfully regulate osteogenic differentiation of stem cells.^[10–12] Among these, optical signals in particular offer a noninvasive way to stimulate local cell responses and promote tissue regeneration.^[13] With controlled experimental parameters, such as power density, pulse duration, and dosage, photobiomodulation (PBM) therapies can switch on or switch off specific signaling pathways, achieving precise cell growth and development regulation with high temporal and spatial resolutions.^[14]

Owing to their large penetration depths in biological tissues, red and near-infrared light have been mostly explored for in vivo PBM, resulting in accelerated tissue healing and mitigated inflammation.^[15] Visible light with shorter wavelengths, however, is also of significant relevance.^[16] Unlike the traditional red and near infrared light, the 420 nm (blue light) and 540 nm (green light) wavelengths are more effective in activating the transient receptor potential cation channel subfamily V member 1 (TRPV1), stimulating osteoblast differentiation and increasing mRNA expression level of osteogenic-related factors compared to 660 and 810 nm.^[17,18] Challenges associated with the application of blue and green light for in vivo PBM stem from their high absorption and scattering losses in tissues. Therefore, their current usage is confined to direct irradiation on superficial tissues,^[19,20] and indirect evoking of systemic regulatory responses via irradiation on visual systems. To facilitate light penetration, optical fibers can be implanted into subdermal regions so as to deliver optical power and signals into the target tissue. Although conventional fibers, mostly made of silica glass, are readily available and can achieve extremely low transmission losses, they are not the ideal solution for bioimplants—their nondegradable and highly rigid structure leads to poor compatibility with biological systems. Optical fibers made of mechanically flexible and biodegradable polymers and hydrogels have been recently exploited as implantable devices for various applications, such as optogenetics, fluorescence photometry, and phototherapy.^[21,22] After completion of the pertinent process, these biocompatible materials are naturally hydrolyzed and absorbed, eliminating the need of retrieval via secondary surgeries.

The purpose of this study was to develop an implantable and biodegradable optical fiber to guide green light into deep tissue defect, and to detect the mechanism of green light regulating bone formation. This study is a continuation of our previous research, which we found blue light and green light promote bone regeneration by regulating calcium concentration in stem cells by in vitro and in vivo experiments.^[18]

Here we explored a green light-based PBM technique with poly(L-lactic acid) & poly(L-lactic-co-glycolic acid) (PLLA&PLGA)-based optical fibers to achieve accelerated bone regeneration. In vitro experiments were performed to explore the effects of green light irradiation on the regulation of osteogenesis of bone marrow-derived mesenchymal stem cells (BMSCs) and corresponding osteogenic-related indicators sensitive to light were identified. Thermally drawn fibers were employed as an optical biointerface, and their optical, thermal, and degradation behaviors were evaluated within tissue. Systematic in vivo studies illustrated the feasibility of fibers for continuous light delivery within 2 weeks.

2. Results and Discussion

2.1. Flexible Degradable Optical Fiber Characterization

Degradable fibers with a diameter of $\approx 200 \mu\text{m}$ were designed to indwell in tissue and degrade along with bone regeneration. Their degradability, optical and thermal properties were characterized accordingly. **Figure 1a–d** showed scanning electron microscopy (SEM) images that illustrated the fiber geometry at the incision (top panel), as well as the surface morphology (bottom panel) at various degradation stages in 95 °C phosphate buffer solution to simulate accelerated degradation environment. The as-prepared fiber exhibited a smooth surface (**Figure 1a**). During the hydrolytic process, the fibers became more brittle and broke after cutting (**Figure 1b,c**). After soaking for 100 h, the fiber broke into pieces and its diameter significantly decreased (**Figure 1d**). Consistent with the geometrical change, the surface roughness of the fiber side also increased with the soaking time during hydrolysis. According to previous research experience, the reaction rate doubled with each 10 °C increase in chemical reaction temperature, so thermal acceleration could be used to illustrate the degradation process of the material, and then the degradation time could be estimated by combining the material's own degradation data.^[23] In order to take consideration to the mechanical strength and light guiding properties, we chose optical fibers soaked for 10 h for in vitro experiments. At this timepoint, the structure of fiber was still completed but the surface was partially decomposed, which was good to facilitate light emission into tissue.

To further evaluate the performance of fibers in the deeper tissue, we investigated the optical and thermal performance of the fiber implanted in a sample of porcine skin (**Figure 1e–g**). We compared the characteristics of a skin sample either illuminated directly with a green laser beam or via an embedded fiber (**F**). **Figure 1h** showed the schematic diagram. **Figure 1e,f** depicted the intensity distribution of green light within the tissue sample with and without the fiber, captured using a digital camera in brightfield and darkfield. The obtained results were in reasonable agreement with Monte Carlo ray-tracing simulations (**Figure 1i**). Without the fiber, the green light penetrated into the tissue at a depth of only $\approx 5 \text{ mm}$; in contrast, the presence of fiber assisted light delivery and optical irradiation could be observed all around the fiber, ensuring that sufficient optical power is delivered into the deep tissue for effective PBM.

Thermal management is an important aspect in phototherapy and needs to be considered when attempting to achieve biocompatibility. Upon laser irradiation, temperature rise in tissues should be carefully monitored so as to prevent unnecessary damage due to heat.^[24,25] **Figure 1g** depicted the temperature distribution, measured by an infrared thermal camera, at different depths in the skin tissue with and without the optical fiber. The experimental results were also verified with finite element simulations, as shown in **Figure 1j**. Under similar input power ($\approx 200 \text{ mW}$), the tissue with an embedded fiber exhibited a much lower temperature-rise ($\Delta T_{\text{max}} = 2.2 \text{ }^\circ\text{C}$) than that directly irradiated with the laser beam ($\Delta T_{\text{max}} = 13.1 \text{ }^\circ\text{C}$). Furthermore, the thermally affected area was much smaller when light was delivered via the fiber. Therefore, we reported that the implanted fiber could help to reduce thermal effects associated with green laser irradiation.

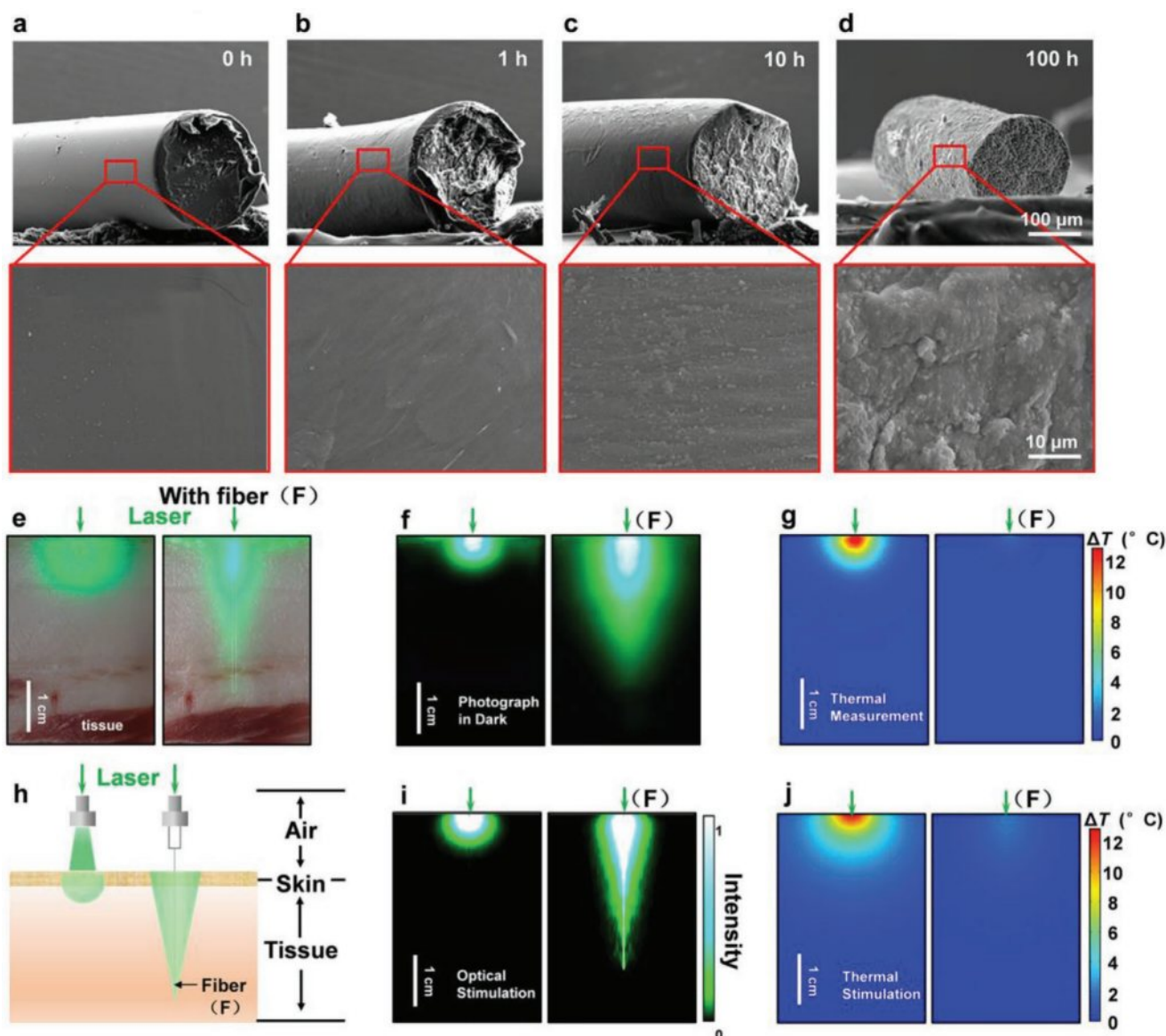


Figure 1. SEM image of the fiber geometry and surface morphology during accelerated degradation a–d). Optical images e) and schematic diagrams h) of the tissues under green laser irradiation, with and without the biodegradable fiber (after soaking for 10 h as c). Measured f) and simulated i) optical power distributions in the tissue. Measured g) and simulated j) temperature distribution in the tissue after emitting for 5 min through both direct and indirect way.

2.2. Biocompatibility and Osteoinductive Capacity of Fibers

To demonstrate the biocompatibility of fibers, BMSCs were cocultured with a fiber for a week. SEM images in **Figure 2a** showed the cell morphology on the fiber surface. The cell shape appeared plump and stretched, with several pseudopods extending out to connect with the fiber surface and surrounding cells. We observed that the fiber was covered with a layer of cells, indicating that they could proliferate and adhere to its surface. In addition, to observe the early adhesion morphology of cells on the surface of the fiber, on Day 3, we performed cellular immunofluorescence staining of the cytoskeletal protein β -tubulin. As evident from **Figure 2b**, the 3D confocal microscopic images revealed that the cells

were evenly attached to the surface of the fiber and retained their healthy state. The growth and morphology of BMSCs proved that fibers and their degradation products had ideal biocompatibility.

Moreover, we tested the mechanical strength of the optical fiber. The bending stiffness of PLLA&PLGA fiber was about $1.5 \times 10^4 \text{ N m}^{-1}$, much smaller than that of conventional fused silica fiber ($2.4 \times 10^5 \text{ N m}^{-1}$) with the same geometry, showing better flexibility and biocompatibility when implanting into tissues. Mechanical properties of the fibers around 37°C were similar among different ratios of PLLA and PLGA (such as 75:25, 65:35, and 50:50).^[22]

Figure 2c compared the osteoinductive effects of fibers themselves and fiber-conducted green light on BMSCs. All

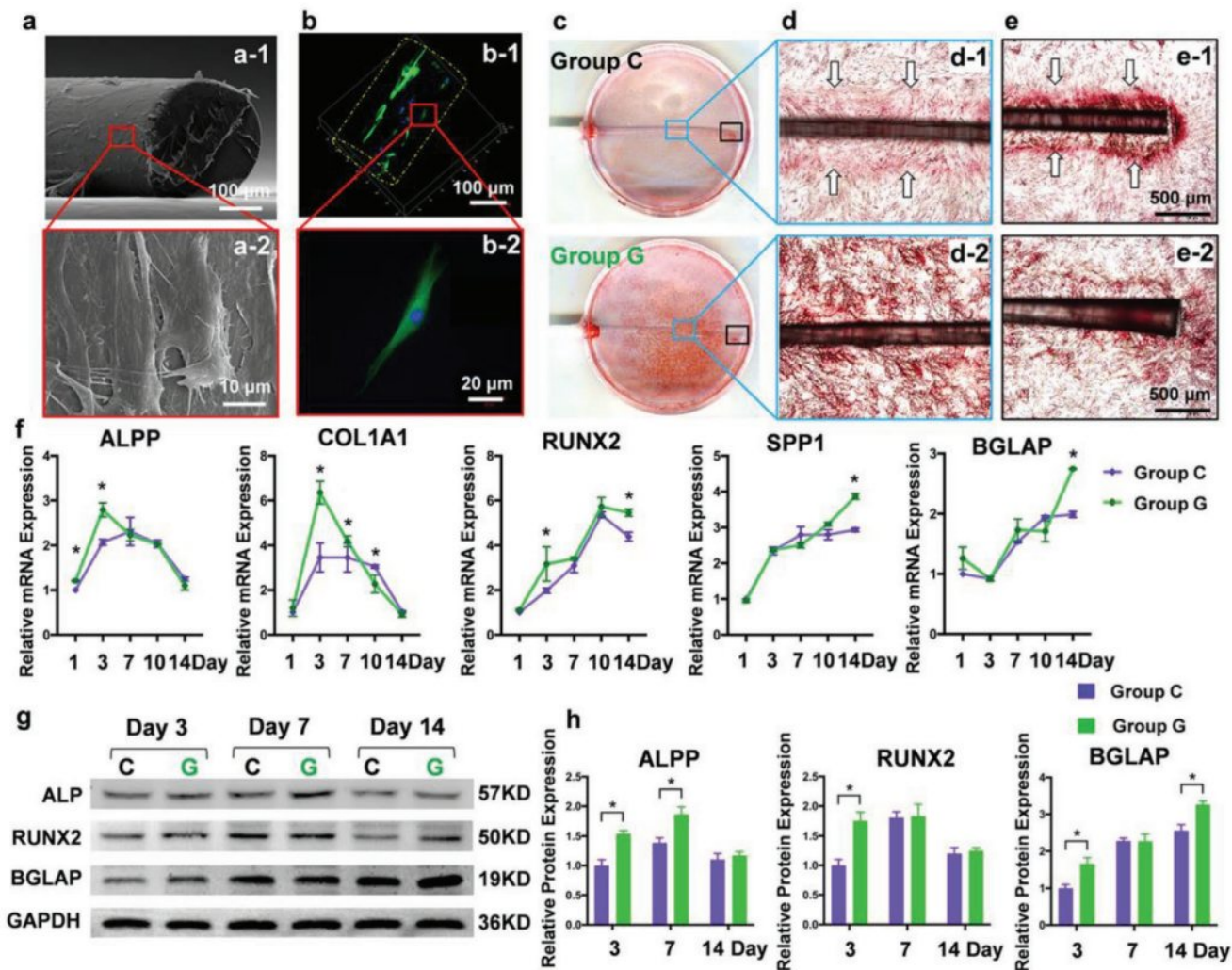


Figure 2. Biocompatibility test of PLLA&PLGA fiber with SEM a) and confocal microscopy b). ARS of BMSCs on the fiber without or with green light illumination c–e). The control group (group C) means no illumination by light, the green light group (group G) receives 520 nm light. mRNA expression of osteogenic related factors f). Protein expression of osteogenic related factors g,h). $n = 3$ in each group; $*p < 0.05$ versus control group.

cell experiments were divided into two groups: the control group (group C) was not illuminated by light, and the green light group (group G) received 520 nm light (25 mW cm^{-2} , 188 s, 1.5 J cm^{-2} , exposure every other day, a total of five times). In group C, calcium nodules increased around the fiber; this phenomenon became more prominent around the tip of fiber where the fiber clung to the bottom of culture dishes (Figure 2e-1). This observation suggested that the degradation products of fibers could promote the osteogenic differentiation of BMSCs, and the osteogenic effect was concentration dependent. The calcium nodules with a deeper color in group G were not only observed around the periphery of the fiber but covered the entire green light conduction range (Figure 2d-2), suggesting that green light could effectively promote BMSC osteogenesis with different physical mechanism from that of chemical promotion of PLLA&PLGA and its degradation products. Considering the dilution of blood, it is difficult to regulate the scope of actions of chemical and biological factors, and their actions are concentration dependent. However,

as a physical stimulation method, green light irradiation can be adjusted in terms of its scope and duration as well as intensity.

The fibers used in this study were filaments with a diameter of only $\approx 200 \mu\text{m}$, which effectively avoided lactic acid accumulation, local pH decrease, and aseptic inflammation, which could be caused upon intensive PLLA and PLGA degradation.

Figure 2f illustrated the phased expression of key osteogenesis-related genes. Alkaline phosphatase, placental (ALPP) is a marker for early osteogenic differentiation. In comparison with group C, green light irradiation upregulated the ALPP expression level on Day 1 and 3. Collagen type I alpha 1 chain (COL1A1) is a marker for extracellular matrix production, and its upregulation indicates the accumulation of bone matrix. We observed that in comparison with group C, green light irradiation upregulated the expression level of COL1A1 on Day 3 and 7 and downregulated it on Day 10, suggesting that green light accelerates collagen production in the early stages of osteogenesis. RUNX family transcription factor 2 (RUNX2) is an osteoblast-specific transcription factor. We observed that

green light irradiation upregulated RUNX2 expression level on Day 10 and 14. Secreted phosphoprotein 1 (SPP1) and bone gamma-carboxyglutamate protein (BGLAP), which are synthesized during the intermediate and late phases of osteogenic differentiation, respectively, are specific markers of osteoblastic maturation. Green light irradiation significantly upregulated the expression levels of both SPP1 and BGLAP on Day 14.

Figure 2g,h showed the protein expression level of osteogenic factors by western blotting (WB) technology. Green light irradiation upregulated the ALPP expression level of BMSCs on Day 3 and 7. The increased expression level of RUNX2 of group G on Day 14 suggested that RUNX2 played a role in promoting osteogenesis by green light. The expression level of BGLAP in both groups increased gradually with time, but green light significantly upregulated BGLAP expression level in the late stage of osteogenesis.

2.3. Green Light Accelerate Bone Regeneration in Femur Defects

In vitro experiments showed that green light irradiation through the fiber accelerated the osteogenesis of BMSCs. Further, to determine whether green light plays the analogous role in vivo, we established a rat bone defect model (cylindrical bone defects with a diameter of 2 mm and a depth of 3.5 mm) to study the effect of fiber-conducted green light on bone repair, fibers were placed in defects of both control groups (group C) and green light groups (group G), but green light was only delivered in group G (Figure 3a–f).

Long bone defect healing commonly includes 4 steps: inflammation, soft callus formation, hard callus development, and bone remodeling.^[26] Micro-CT can provide high-resolution 2D and 3D images and bone mineral density measurements to visualize and quantify new bone formation in the bone defect area. Taking the fiber as the central axis, a cylindrical region of interest with a

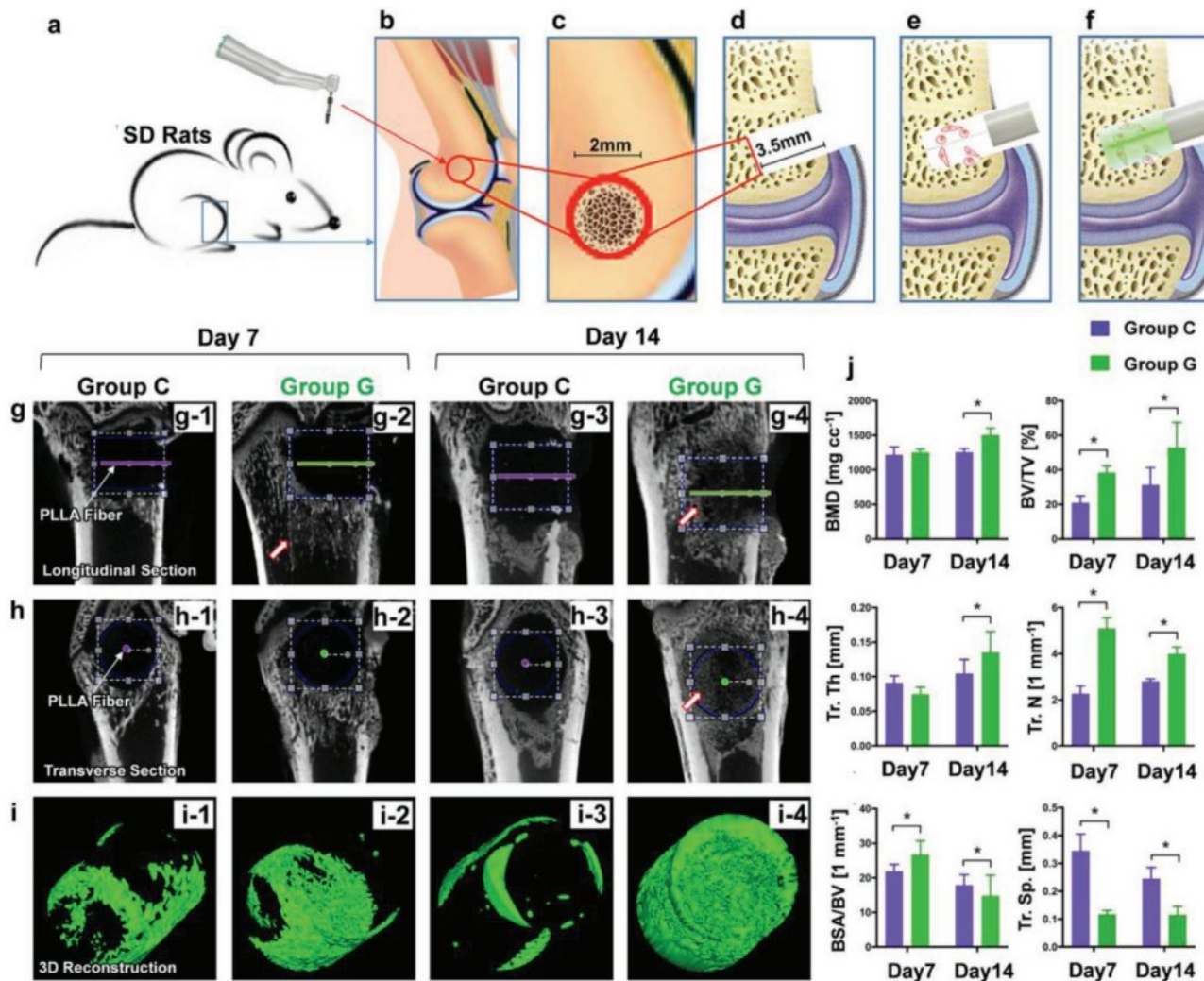


Figure 3. Diagram of the SD rat bone defect model established procedure a–f). Optical fibers are placed in both groups, the control group (group C) means no illumination and green light group (group G) receives 520 nm light. The longitudinal section of the femur with PLLA&PLGA fiber as the central axis g). The transverse section of the femur with the fiber as the central axis, Little center circles are the fiber position, and red arrows indicate new trabecular bone growth in the direction of light h). Representative 3D micro-CT images within a region of interest (ROI) of central 3 mm in diameter of the bone tunnel i). Quantitative analysis of micro-CT of the new bone in ROI j). *n* = 5 in each group; **p* < 0.05 versus control group.

diameter of 3 mm and height of 3.5 mm were selected. 2D images showing the parallel (Figure 3g) and the vertical (Figure 3h) direction of the fiber were taken. 3D reconstruction of the fiber with bone morphology indicators was shown in Figure 3i.

On Day 7, the bone defect was noted to be undergoing active reconstruction. Within the range of the bone defect, low-density images were obtained for both the groups, suggesting no new bone formation (Figure 3g,h). However, in group G, several parallel lines of increased bone density in the bone marrow cavity were evident below the bone defect (indicated by an arrow), resembling the growth of the new trabecular bone (Figure 3g-2). This phenomenon implied that green light might have stem cell recruitment effects, causing distant BMSCs to migrate to the bone defect area. On Day 14, no trabecular bone that reached the threshold of the X-ray detectable range was detected within the bone defect area in group C (Figure 3h-3). In group G, however, several new trabecular bones were observed to be arranged around the fiber with increased bone density (Figure 3h-4). In Figure 3i, 3D reconstruction images showed no obvious difference between two groups in terms of bone morphology and volume on Day 7, but a large number of fine trabeculae filled the entire bone defect area on Day 14 in group G.

As shown in Figure 3j, we measured bone morphological structures in terms of following characteristics: bone mineral density (BMD), bone volume/total volume (BV/TV), trabecular thickness (Tb. Th), trabecular number (Tb. N), bone surface area/bone volume (BSA/BV), and trabecular spacing (Tr. Sp.). BMD results illustrated that the BMD of both groups increased with time, with the values for group G significantly higher than those for group C on Day 14 ($p < 0.05$). BV/TV is the percentage of trabecular BV to TV, which can reflect bone mass. In comparison with group C, BV/TV, and Tb. Th of group G increased with time, while Tb. N gradually decreased, indicating that trabecular bones might merge with an increase in thickness. Therefore, the thickness and volume of the trabecular bone were noted to increase, while the number decreased.

Furthermore, taking the fiber as the central axis, morphological characteristics were performed by hematoxylin-eosin (H&E) staining, Masson's Trichrome staining (Masson), immunohistochemical staining (IHC), and tartrate-resistant acid phosphatase (TRAP) staining (Figure 4).

H&E staining indicated no new bone formation in both groups on Day 7 (Figure 4a1-2). Higher nonspecific chronic inflammatory process was detected inside the bone defect with the presence of plasma cells, lymphocytes, and macrophages in group C, lower rates of inflammatory infiltrates were observed in group G (Figure 4a1-2). On Day 14, we observed a large number of fine irregular trabecula around the fiber in group C (Figure 4a-3). They were scattered and not clearly connected, implying that only the bone matrix had formed and that calcium salt deposition had yet to occur. Therefore, micro-CT showed no trabecular architecture in group C on Day 7. In contrast, radial and interconnected thick trabecular bones were observed around the fiber in group G (Figure 4a-4).

Masson staining presented no bone trabecula formation in either group on Day 7. On Day 14, increased amount of collagen sponge (blue) was observed in group C, while group G formed a large amount of immature collagen (light blue) around the

fiber and thick-interconnected bone trabecula in periphery (Figure 4b).

Immunohistochemistry indicated that BGLAP expression on Day 14 in group G was much higher than that in group C (Figure 4c-4), which validated our RT-qPCR (reverse transcription quantitative real-time polymerase chain reaction (PCR) and WB results, indicating that green light could promote BGLAP expression both in vitro and in vivo. TRAP staining showed the presence of osteoclasts on Day 7 as well as 14, but there was no obvious difference in cell number and morphology (Figure 4d), which indicated that green light may not affect osteoclasts.

2.4. Mechanism of Green Light on Osteogenesis

To explore the possible mechanism of green light on the osteogenesis of BMSCs, we performed WB to detect the dynamic expression of phosphorylated extracellular signal-regulated kinases (P-ERK) and RUNX2 at various time points throughout the osteogenesis (Figure 5a). Green light-emitting diode (530 nm) irradiation increased human orbital fat stem cells migration through activation of ERK/MAP kinase/p38 signaling pathway.^[27] P-ERK might bind to the promoter domains of BGLAP in osteoblasts via the association between RUNX2 and ERK.^[28] P-ERK in group C expressed relatively stable, RUNX2 increased until Day 6 and then decreased (Figure 5b). P-ERK and RUNX2 of Group G continued to increase on Day 10 and 14, suggesting that green light might activate P-ERK and regulate downstream osteogenic transcription factor RUNX2.

3. Conclusions

Although the mechanism underlying such a PBM process demands further investigations at the molecular and cellular levels, we have demonstrated its efficacy via both in vitro and in vivo experiments. Here we discovered that visible light, particularly green light, plays an important role in osteogenesis by regulating BGLAP and RUNX2 expression levels in BMSCs. To deliver green light into deep tissues, we employed optical fibers as a biodegradable implant, which promoted bone defect regeneration in a rodent model. In case of conventional water-soluble polymers, such as PLLA, one of the limitations is their natural, uncontrollable hydrolysis, leading to gradual performance deterioration during the treatment process. Possible solutions include the use of a cladding layer on the fiber surface or engineering a synthetic polymer with controlled degradation in a triggered manner. For complicated bone defects with a large volume, the cylindrical fibers used in this study are not ideal, as light cannot be easily delivered via them into the entire bone defect region. In such a scenario, we envision that customized fiber structures fabricated by 3D printing could be employed for effective optical coverage.^[29] In addition, these optical fibers should be made to cooperate with recently developed electronic sensors with similar degradation behaviors,^[30] forming fully integrated close-loop systems to monitor and regulate the regeneration status in real time. In the future, such an optical treatment can also be combined with the administration of

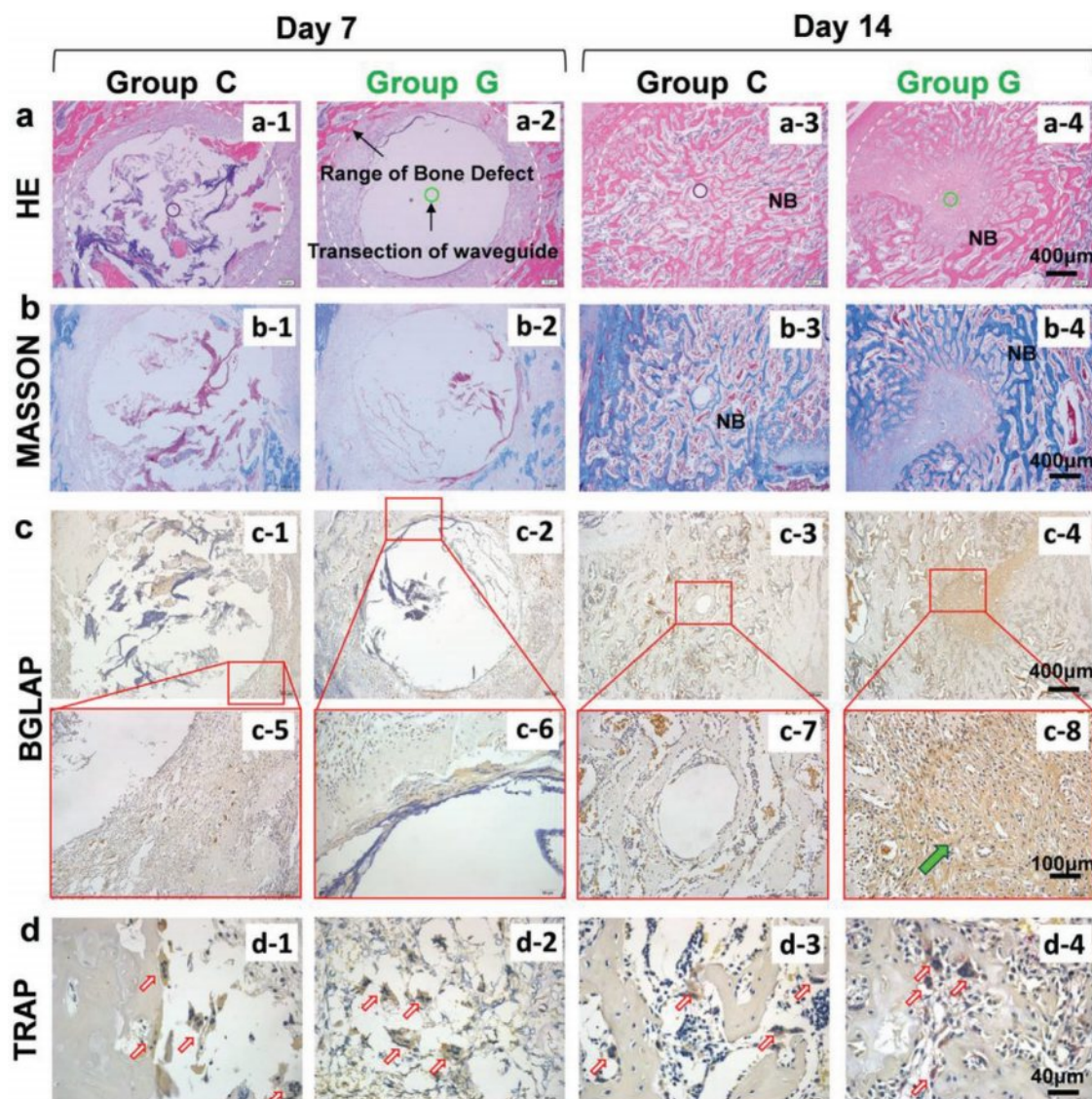


Figure 4. Images of histochemical staining by H&E to show newly generated bone tissue and inflammatory cell infiltrations of group C and group G a). The white dotted circle is the outline of bone defect; small circles in the center locates optical fibers; NB-marked pink homogeneous structure is new bone matrix. and Masson b) IHC staining locates BGLAP shown by brown staining and marked by green arrows c). TRAP staining of osteoclasts located by red arrows d).

photosensitive medicine, growth factor, and stem cell therapy for tissue regeneration.^[31] Working together with advanced biodegradable optical devices, the PBM technique provides a generic solution to tissue regeneration, holding great promise in clinical applications.

4. Experimental Section

Fabrication and Characterization of PLLA&PLGA Fibers: PLLA and PLGA are Food and Drug Administration-approved biodegradable polymers with excellent physicochemical properties and biocompatibility; moreover, it has suitable biodegradability and its degradation products are harmless.^[32]

PLLA&PLGA ($M_w = 55\,000$ Da) was purchased from Jinan Daigang Biomaterial Co., Ltd., the molecular weight of which was adjusted to

match the degradation rate with the osteogenesis process. The raw material mixture was heated to 220 °C and subsequently drawn using glass tubes. The fiber diameter was controlled by the speed of drawing; fibers with a diameter of $\approx 200\ \mu\text{m}$ were applied for in vitro and in vivo experiments.

To elucidate the evolution of fiber morphology at various stages of degradation, fibers were soaked in phosphate-buffered saline (PBS) solution (pH 7.4) at 95 °C for 1, 10, and 100 h, rinsed with deionized water, and dried. Fibers were then cut and analyzed using a scanning electron microscope (Zeiss Merlin FE-SEM).

3D optical models were built using the Monte Carlo ray-tracing method (TracePro, Lambda Research Corporation, USA). Fiber geometry was the same as that in the experiments, and optical properties of PLLA&PLGA were applied. The light source was defined as a random distribution of 10^5 rays, and monitors were used to measure light distribution at different depths. At the wavelength of 520 nm, the simulated dermis tissue in the model had a refractive index of 1.37,

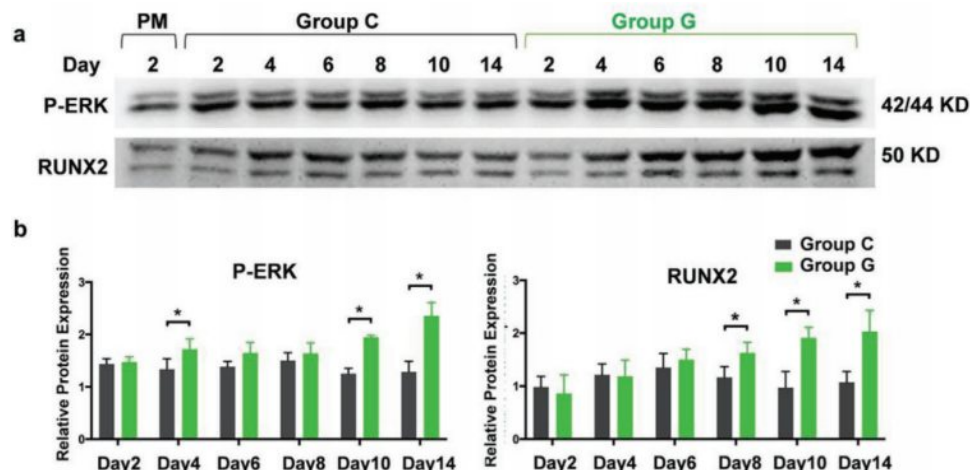


Figure 5. The protein expression level of P-ERK and RUNX2 of BMSC on Day 2, 4, 6, 8, 10, and 14 during osteoinducing a). Quantitative evaluation of p-ERK and Runx2 expression b).

scattering coefficient of 18.7 mm^{-1} , anisotropy factor of 0.81, and absorption coefficient of 0.3 mm^{-1} .

3D stationary radiation and heat transfer models were established using the finite element analysis method (COMSOL Multiphysics). The model accounted for the radiation and heat transfer through the tissue as well as natural heat convection. The light intensity in the fiber, which was obtained in optical simulation, and the laser irradiation on the tissue surface served as the radiation source for tissues with and without fibers, respectively. The optical properties were the same as those in optical simulation. Moreover, the tissue in this model had a heating capacity of $3391 \text{ J kg}^{-1} \text{ K}^{-1}$, density of 1109 kg m^{-3} , and thermal conductivity of $0.37 \text{ W m}^{-1} \text{ K}^{-1}$.

In Vivo Bone Defect Remolding Study: 20 12-week-old male Sprague Dawley rats (SD rats, Chauncey Biology, China) were randomly assigned to the C and G groups (10 rats per group). Five rats per group were asphyxiated by excessive inhalation of CO_2 at two timepoints (Day 7 and 14) each. This study design was approved by the Institutional Review Board of Peking University Health Science Center (LA2018176).

First, rats were anesthetized with 1% pentobarbital sodium via an intraperitoneal injection. After exposing the distal femur via a skin incision and blunt dissection, a cylindrical hole (depth, 3.5 mm; diameter, 2 mm) was vertically drilled through the cortical bone in each distal femur under cooling conditions with saline water. The approximate distance between the hole and distal femur growth plate was 2–3 mm. A ceramic holder with a 3 mm fiber protruding from it was inserted into the bone defect. The muscular fascia, subcutaneous tissue, and skin were then sutured around the holder in sequence (Figure 3a–f).

Group G was illuminated through the ceramic holder every other day, starting at the second day postsurgery, five times in total. A homogenized laser source (520 nm green light, Laserwave, China) was placed stable, the full power density of green light irradiation through the fiber on the tissue was 25 mW cm^{-2} . Other than green light irradiation, all procedures for group C were consistent with those for group G. The animals were excluded if the ceramic holder detached; at least three qualified samples were analyzed from each group per timepoint. The femurs were eventually detached and fixed in 10% v/v neutral buffered formalin for use in subsequent experiments.

Micro-CT (Inveon MM CT, SIEMENS, Germany) was used to scan the harvested femurs, and Cobra Exxim (EXXIM Computing Corp., CA) was used to analyze and reconstruct the 2D and 3D models. The newly formed bone structures were analyzed using Inveon Research Workplace (SIEMENS).

After ethylene diamine tetraacetic acid (Thermo Fisher Scientific) decalcification and gradient alcohol dehydration, the femurs were embedded in paraffin. The sectioning direction was perpendicular

to the direction of the fiber, and the slice thickness was 4 μm . H&E, Masson (G1345, Solarbio, China), IHC (OPG-antibody, 1:200, GB13152; BGLAP-antibody, 1:100, GB11233 Servicebio, China), and TRAP staining (387A, Sigma) were performed according to standard procedures using commercial kits.

Experiments In Vitro: Human BMSCs (#7500, ScienceCell, USA) were cultured in mesenchymal stem cell medium (MSCM, #7510, ScienceCell), and subculture was performed until the culture reached $\approx 80\%$ confluence. The cells between passage 5 and 8 were seeded into culture dishes (diameter, 3.5 cm; used for all cell inoculation experiments in this study) (BEAVER, China) at a density of $\approx 1 \times 10^5$ cells per dish. MSCM was changed every 48 h.

The side wall of culture dishes was drilled and a ceramic holder was inserted into the hole; the holder was fixed in the downward direction using an instant adhesive, which ensured that the front end of the fiber clung to the bottom of the dish.

BMSCs were seeded onto fibers in a dish and cultured for 3 d. After 4% paraformaldehyde (Solarbio) fixing and 1% Triton X-100 (Solarbio) cell membrane permeabilization, BMSCs were incubated with β -tubulin-antibody (1:1000, 66240-1-Ig, Proteintech) overnight on a shaker at 4 $^\circ\text{C}$. Subsequently, the cells were incubated with a fluorescent secondary antibody (1:500, SA00001-1, Proteintech) for 1 h at room temperature. The fiber was then carefully cut into sections with a length of ≈ 4 mm placed between two pieces of high transparency cover glasses with 10 μL 4',6-diamidino-2-phenylindole (DAPI, Solarbio). Images of cocultured cells using confocal microscopy (LSM710, ZEISS, Germany) were ultimately captured.

BMSCs were seeded into culture dishes (diameter, 3.5 cm) at a density of $\approx 1 \times 10^5$ cells per dish. After incubation for 4 h at 37 $^\circ\text{C}$ and 5% CO_2 , MSCM was removed and replaced with osteogenic-inducing medium (OM), which was Dulbecco's modified Eagle's medium (Gibco, USA) containing 10% fetal bovine serum (Gibco), 1% penicillin–streptomycin (Gibco), $200 \times 10^{-6} \text{ M}$ L-ascorbic acid (Sigma, USA), $10 \times 10^{-3} \text{ M}$ β -glycerophosphate disodium (Sigma), and $100 \times 10^{-9} \text{ M}$ dexamethasone (Sigma). OM was changed every 48 h. OM was replaced the next day after cell seeding and alizarin red S (ARS) staining was performed at Day 10 for both groups C and G. The laser emission power from fibers was 25 mW cm^{-2} .

ARS (Sigma) staining was performed to evaluate the formation of mineralized nodules on Day 10 and 14. BMSCs were fixed in 4% paraformaldehyde (Solarbio, China) for 10 min. After rinsing with PBS (Solarbio), the cells were incubated in 1% ARS dye for 20 min. Subsequently, excess ARS dye was removed with deionized water, and images of the specimens were captured using a scanner. For quantitative detection, the ARS-stained samples were then incubated in

Table 1. Primer sequences.

Gene name	Primer	Sequences (5' to 3')
GAPDH	Forward	GAAGGTCGGAGTCAACGGATT
GAPDH	Reverse	TGACGGTGCCATGGAATTTG
ALPP	Forward	GTACGAGCTGAACAGGAACAACG
ALPP	Reverse	CTTGGCTTTTCTTCATGGTG
COL1A1	Forward	CTCCTGACGCACGGCC
COL1A1	Reverse	CCGTTCTGTACGCAGGTGATT
RUNX2	Forward	GCTTCCTGCCATACCGA
RUNX2	Reverse	TCAGTGAGGGATGAAATGCTTG
SPPI	Forward	AGAAGTTTCGACACCTGACATC
SPPI	Reverse	GATGGCCTTGATGCACCATT
BGLAP	Forward	CACTCCTGCCCTATTGGC
BGLAP	Reverse	CCCTCCTGCTGGACACAAG

1% hexadecylpyridinium chloride monohydrate (Sigma) for 2 h and the absorbance was monitored at 550 nm using a microplate reader (BioTek, BioTek Instruments, USA).

mRNA was isolated from BMSCs using TRIzol (Invitrogen, USA) at Day 1, 3, 7, 10, and 14. Reverse transcription was performed using a PrimeScript RT reagent kit (TaKaRa, Japan), and RT-qPCR was conducted on a real-time fluorescent quantitative PCR instrument (QuantStudio 3, Thermo Fisher Scientific, USA) using the SYBR green dye (Roche, USA). The primers are listed in **Table 1**. Glycerinaldehyde-3-phosphate dehydrogenase (GAPDH) was used as the housekeeping gene. Osteogenic-related factors (ALPP, COL1A1, RUNX2, SPPI, and BGLAP) were detected by RT-qPCR.

For WB detection, BMSCs were lysed using 40 μ L radioimmunoprecipitation assay buffer (Solarbio) on Day 3, 7, and 14 and centrifuged at 12 000 rpm for 30 min. The supernatant was collected, and protein concentration was quantified using the bicinchoninic acid protein assay kit (Thermo Fisher Scientific); absorbance was measured at 562 nm using a microplate reader. The protein loading quantity was 20 μ g. Constant pressure electrophoresis was performed at 80 V until the protein marker completely separated. Protein bands were then transferred onto nitrocellulose membranes at a constant pressure of 80 V for 1 h. The membranes were blocked in 5% nonfat milk in tris-buffered saline tween-20 for 1 h at room temperature before overnight incubation at 4 °C with antibody of ALPP (1:1000, abs135024a, Absin, China), RUNX2 (1:2000, abs131274a, Absin), BGLAP (1:1000, abs104146, Absin), p-ERK (1:1000, 4370, CST, USA), GAPDH (1:2000, 10494-1-AP, Proteintech, USA). Visualization was performed using secondary antirabbit antibody (1/10 000, SA00001-2, Proteintech) followed by electrochemiluminescence reagent (ECL, NCM Biotech, China) by the multifunction imager (Fusion Fx, VILBER, France).

Statistical Analyses: Statistical analysis was performed with SPSS version 22.0. Unpaired *t*-test was used for comparison between different groups at the same time. One-way analysis of variance was used for different timepoints of the same group. *p* < 0.05 indicated statistical significance.

Acknowledgements

Y.J., W.Q., and Q.Z. contributed equally to this work. Q.Z. and L.Y. acknowledge the support from Tsinghua University-Peking Union Medical College Hospital Initiative Scientific Research Program (20191080592). X.S. acknowledges the support from Beijing Innovation Center for Future Chips, Tsinghua University, Beijing National Research Center for Information Science and Technology at Tsinghua University (BNR2019ZS01005), State Key Laboratory of Advanced Optical Communication Systems and Networks (2018GZKF03005), and Beijing Municipal Natural Science Foundation (4202032). Y.W. acknowledges the support from the National Natural Science Foundation of

China (51972003), Peking University Health Science Center Project Beijing High Precision Discipline (BMU2019GJJK024), Sub-project of National Key Research and Development Plan (2018YFE0192500), Clinical Characteristics Application of Research Projects in Capital (Z181100001718186), Smart Medical Discipline Construction Project in Peking University Health Science Center (BMU2018ZHYL013), New Technology and New Therapy Project in Peking University School of Stomatology (PKUSSNCT-16A06). H.L. acknowledges the support from the National Natural Science Foundation of China (81700935). This paper is dedicated to the memory of the late Professor Peijun Lyu.

Conflict of Interest

The authors declare no conflict of interest.

Keywords

biodegradable devices, optical fibers, osteogenesis, photobiomodulation, tissue regeneration

Received: December 22, 2019

Revised: February 19, 2020

Published online: April 7, 2020

- [1] J. Pizzicannella, S. D. Pierdomenico, A. Piattelli, G. Varvara, L. Fonticoli, O. Trubiani, F. Diomedede, *Materials* **2019**, *12*, 2157.
- [2] D. A. Behrends, D. Hui, C. Gao, A. Awlia, Y. Al-Saran, A. Li, J. E. Henderson, P. A. Martineau, *Clin. Orthop. Relat. Res.* **2017**, *475*, 906.
- [3] N. Marsden, K. Shokrollahi, K. Maw, A. Sierakowski, F. Bhat, B. Mathur, *Ann. R. Coll. Surg. Engl.* **2010**, *92*, W18.
- [4] Z. Chen, A. Bachhuka, S. Han, F. Wei, S. Lu, R. M. Visalakshan, K. Vasilev, Y. Xiao, *ACS Nano* **2017**, *11*, 4494.
- [5] B.-B. Seo, J.-T. Koh, S.-C. Song, *Biomaterials* **2017**, *122*, 91.
- [6] S. Ali Akbari Ghavimi, B. N. Allen, J. L. Stromsdorfer, J. S. Kramer, X. Li, B. D. Ulery, *Biomed. Mater.* **2018**, *13*, 055005.
- [7] T. Liu, Y. Zheng, G. Wu, D. Wismeijer, J. L. Pathak, Y. Liu, *Sci. Rep.* **2017**, *7*, 41800.
- [8] M. Bouyer, R. Guillot, J. Lavaud, C. Pletinx, C. Olivier, V. Curry, J. Boutonnat, J.-L. Coll, F. Peyrin, V. Jossierand, G. Bettega, C. Picart, *Biomaterials* **2016**, *104*, 168.
- [9] W. Shi, M. Sun, X. Hu, B. Ren, J. Cheng, C. Li, X. Duan, X. Fu, J. Zhang, H. Chen, Y. Ao, *Adv. Mater.* **2017**, *29*, 1701089.
- [10] J. J. Leskinen, A. Olkku, A. Mahonen, K. Hynynen, *IEEE Trans. Biomed. Eng.* **2014**, *61*, 920.
- [11] P. Li, J. Xu, L. Liu, Y. Zhang, M. Liu, Y. Fan, *J. Biomed. Nanotechnol.* **2019**, *15*, 921.
- [12] R. Mikami, K. Mizutani, A. Aoki, Y. Tamura, K. Aoki, Y. Izumi, *Lasers Surg. Med.* **2018**, *50*, 340.
- [13] X. Xu, X. Liu, L. Tan, Z. Cui, X. Yang, S. Zhu, Z. Li, X. Yuan, Y. Zheng, K. W. K. Yeung, P. K. Chu, S. Wu, *Acta Biomater.* **2018**, *77*, 352.
- [14] G. B. Ates, A. E. Ak, B. Garipcan, M. Gülsoy, *Lasers Med. Sci.* **2017**, *32*, 1847.
- [15] A. Yadav, A. Gupta, *Photodermatol., Photoimmunol. Photomed.* **2017**, *33*, 4.
- [16] L. A. Trotter, D. Patel, S. Dubin, C. Guerra, V. McCloud, P. Lockwood, R. Messer, J. C. Wataha, J. B. Lewis, *Photochem. Photobiol. Sci.* **2017**, *16*, 883.
- [17] Y. Wang, Y.-Y. Huang, Y. Wang, P. Lyu, M. R. Hamblin, *Sci. Rep.* **2017**, *7*, 7781.
- [18] Y. Wang, Y.-Y. Huang, Y. Wang, P. Lyu, M. R. Hamblin, *Sci. Rep.* **2016**, *6*, 33719.

- [19] N. Yu, L. Huang, Y. Zhou, T. Xue, Z. Chen, G. Han, *Adv. Healthcare Mater.* **2019**, *8*, e1801132.
- [20] M. M. Ibrahim, A. Patwardhan, K. B. Gilbraith, A. Moutal, X. Yang, L. A. Chew, T. Largent-Milnes, T. P. Malan, T. W. Vanderah, F. Porreca, R. Khanna, *Pain* **2017**, *158*, 347.
- [21] Q. Wang, D. Yuan, W. Liu, J. Chen, X. Lin, S. Cheng, F. Li, X. Duan, *Med. Sci. Monit.* **2016**, *22*, 362.
- [22] R. Nazempour, Q. Zhang, R. Fu, X. Sheng, *Materials* **2018**, *11*, 1283.
- [23] J. Shin, Y. Yan, W. Bai, Y. Xue, P. Gamble, L. Tian, I. Kandela, C. R. Haney, W. Spees, Y. Lee, M. Choi, J. Ko, H. Ryu, J.-K. Chang, M. Pezhohou, S.-K. Kang, S. M. Won, K. J. Yu, J. Zhao, Y. K. Lee, M. R. MacEwan, S.-K. Song, Y. Huang, W. Z. Ray, J. A. Rogers, *Nat. Biomed. Eng.* **2019**, *3*, 37.
- [24] P. S. Yarmolenko, E. J. Moon, C. Landon, A. Manzoor, D. W. Hochman, B. L. Viglianti, M. W. Dewhirst, *Int. J. Hyperthermia* **2011**, *27*, 320.
- [25] J. W. Fisher, S. Sarkar, C. F. Buchanan, C. S. Szot, J. Whitney, H. C. Hatcher, S. V. Torti, C. G. Rylander, M. N. Rylander, *Cancer Res.* **2010**, *70*, 9855.
- [26] M. S. Ghiasi, J. Chen, A. Vaziri, E. K. Rodriguez, A. Nazarian, *Bone Rep.* **2017**, *6*, 87.
- [27] W.-K. Ong, H.-F. Chen, C.-T. Tsai, Y.-J. Fu, Y.-S. Wong, D.-J. Yen, T.-H. Chang, H.-D. Huang, O. Kuang-Sheng Lee, S. Chien, J. H.-C. Ho, *Biomaterials* **2013**, *34*, 1911.
- [28] Y. Li, C. Ge, R. T. Franceschi, *J. Bone Miner. Res.* **2010**, *25*, 154.
- [29] K. Cook, J. Canning, S. Leon-Saval, Z. Reid, Md. A. Hossain, J.-E. Comatti, Y. Luo, G.-D. Peng, *Opt. Lett.* **2015**, *40*, 3966.
- [30] M. Yao, X. Ouyang, J. Wu, A. P. Zhang, H.-Y. Tam, P. K. A. Wai, *Sensors* **2018**, *18*, 1825.
- [31] J. Venkatesan, S. Anil, S.-K Kim, M. S. Shim, *Int. J. Biol. Macromol.* **2017**, *104*, 1383.
- [32] P. Simamora, W. Chern, *J. Drugs Dermatol.* **2006**, *5*, 436.